

Chapter 1

Introduction

1.1 Charge Transport in Organic Semiconductors

1.1.1 Organic Semiconductors

Conductive polymers were first discovered in 1977 by Shirakawa et al^{6,7} for which they were awarded the Nobel prize in Chemistry. Recently these materials have become ubiquitous in many technologies, such as in organic photovoltaic cells⁸, organic field-effect transistors (OFET)⁹ and organic light-emitting diodes (OLED)¹⁰. While the other two technologies lag behind their inorganic counterparts, uptake of OLED screens is becoming ubiquitous -especially in the smartphone and television market due to their flexibility, better colour representation and lower energy consumption than standard backlit LCD displays. OLEDs have also found uses in lighting with their efficiency rivalling that of fluorescent tubes^{11,12}. Although, industry has made large strides in fabricating and using these materials the exact nature of the charge transport is still poorly understood. Traditional theories (such as hopping and band transport) aren't applicable to many relevant materials¹³⁻¹⁷ as charge transfer dynamics lies in an intermediate region where the polaron is neither fully localised or delocalised. This is due to crystals typically being formed of organic molecules weakly held together by Van der Waals (VDW) forces rather than strong covalent bonds. This allows molecules to fluctuate about their lattice sites and introduces a disorder that doesn't appear in inorganic crystals.

In order to properly quantify the performance of organic semiconductors a key prop-

erty is the charge carrier mobility. Typically, charge carrier mobilities in ‘good’ organic semiconductors (OSCs) fall between 1-10 $\text{cm}^2\text{V}^{-1}\text{s}^{-1}$ ¹⁸. Though higher mobilities, in pure crystals such as Rubrene, have been recorded in the range 15-20+ $\text{cm}^2\text{V}^{-1}\text{s}^{-1}$ ^{19,20}. This is beyond the range of hopping model validity ($\sim 1 \text{ cm}^2\text{V}^{-1}\text{s}^{-1}$) and below that of band theory ($> 50 \text{ cm}^2\text{V}^{-1}\text{s}^{-1}$)¹⁷. In this intermediate regime the charge carriers are typically not completely delocalised at the valence band edges (band regime) or localised to a single site/molecule (hopping regime) but delocalised over a few/tens of molecules²¹. Without any analytic approaches currently being valid in this regime many atomistic computational approaches have been developed to investigate the underlying charge transport mechanisms²².

1.2 Atomistic Simulations of Nonadiabatic Processes

In simulating processes involving electronic transfers a key approximation used in conventional molecular dynamics (MD) breaks down. That is the Born-Oppenheimer or adiabatic approximation²³. This approximation, relied upon for almost a century²⁴, hinges on the fact that nuclei are much more massive than electrons and are approximately stationary with respect to electron movement²⁵. This results in nuclear evolution that is governed by a single, adiabatic, potential energy surface. However, in many interesting processes, such as the proton coupled electron transfer in photosynthesis and respiration²⁶⁻²⁸, non-radiative decay and photochemical processes, electronic transitions between adiabatic potential energy surfaces occur²⁹. Simulating these processes requires non-adiabatic molecular dynamics (NAMD) techniques to be developed, to correctly capture dynamical properties.

There have been many techniques proposed for use in NAMD such as the quantum classical Liouville equation³⁰, multiple spawning³¹ or nonadiabatic Bohmian dynamics³². However, two of the most popular are trajectory surface hopping³³ and mean-field approaches³⁴. This is probably due to their relative simplicity to implement, efficiency for

large systems and proven efficacy in a wide variety of situations³⁵. In these approaches the general aim is to treat as much of the system as possible with (computationally cheaper) classical mechanics. While handling all necessary parts with quantum mechanics³⁶. In Surface Hopping, Ehrenfest and Coupled-Trajectory Mixed Quantum-Classical molecular dynamics (CTMQC) one treats the nuclear subsystem classically and the electronic one quantum mechanically. The nuclei are normally propagated using a velocity verlet algorithm according to Newton's laws and electrons using a fourth order Runge Kutta algorithm according to the time-dependent Schrödinger equation. The wavefunction is normally expanded as a linear combination of adiabatic or diabatic states. The nuclei and electrons can also interact. Taking account of this interaction is where these techniques differ. No one technique is perfect, the issues for surface hopping and Ehrenfest are well documented and have been discussed in detail^{37–41}. CTMQC is a fairly new technique and its issues are still mostly unknown. In this document I will discuss CTMQC in depth and present results from my own implementation of it as well as presenting its drawbacks. I will also compare these results to Ehrenfest and Trajectory Surface Hopping (TSH).

1.2.1 Surface Hopping and Ehrenfest Dynamics

An important technique in the field of mixed quantum classical nonadiabatic molecular dynamics is Ehrenfest dynamics. Assuming we treat the nuclei classically the Ehrenfest equations can be rigorously derived from the electronic Schrödinger equation. This is done by assuming that the nuclei's motion is provided by a single population weighted average potential energy surface. This average is taken from the adiabatic potential energy surfaces (eigenvalues of the Hamiltonian) where weights are provided by the populations of each adiabatic state. This effective potential energy surface is shown in fig 1.1. In this way the electronic

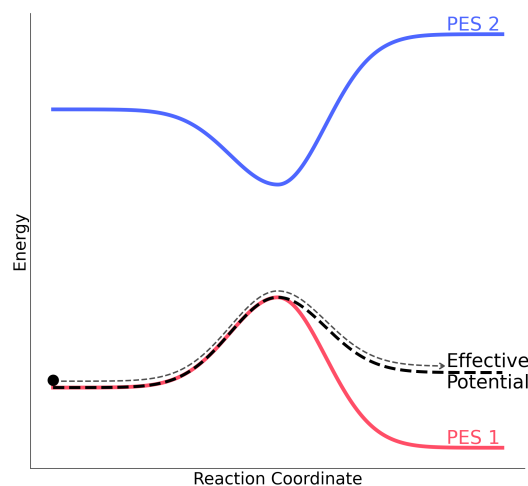


Figure 1.1: An example of a typical Ehrenfest simulation near an avoided crossing. The black lines represent the adiabatic potential energy surface due to the ground (PES 1) and excited (PES 2) state. The red line represents the population weighted average potential the nuclei travel on.

subsystem influences the propagation of the nuclei. The propagation of the forces and the electrons are controlled by equations (1.1) and (1.2).

$$F_{\mathbf{v}}^{Ehren} = \sum_i^{N_{st}} |C_i|^2 \nabla_{\mathbf{v}} E_i + \sum_{i,j}^{N_{st}} C_i^* C_j (E_j - E_i) \mathbf{d}_{ij,\mathbf{v}} \quad (1.1)$$

$$\hbar \dot{\mathbf{C}}_m = C_m E_m - i \hbar \sum_n^{N_{st}} C_n d_{mn}^{ad} \quad (1.2)$$

In the above equations C_i is the adiabatic expansion coefficient for state i , E_m is the energy of adiabatic state m , $\mathbf{d}_{mn,\mathbf{v}}^{ad}$ is the nonadiabatic coupling (in the adiabatic basis) between states m and n for atom \mathbf{v} . The d_{mn}^{ad} are the nonadiabatic coupling elements expressed in the adiabatic basis. Although the Ehrenfest method has been applied with success in many systems^{42–44} it has a number of key shortcomings. Namely, its inability to capture the branching of the nuclear wavefunction as propagation occurs on only a single potential energy surface and its poor account of the decoherence of the electronic and nuclear subsystem after an avoided crossing. Ehrenfest also violates detailed balance by populating all adiabatic states evenly^{23,45}. In the limit of infinite states this results in infinite electronic temperature⁴⁶. Possibly the most popular technique in NAMD is trajectory surface hopping. In trajectory surface hopping the shape of the potential energy surface is determined by a series of discrete stochastic hops between adiabatic potential energy surfaces⁴⁵. See fig 1.2. The probability of these hops is determined by the non-adiabatic coupling between states. A swarm of trajectories are used and the probability a hop (non-adiabatic coupling) determines how many of these change state. The nuclear dynamics are dictated by the shape of the energy surface they are travelling on. This method can capture the branching of nuclear wavepacket unlike Ehrenfest. However, it still suffers from a number of issues. The original ‘fewest switches surface hopping’ proposed by John Tully suffered from bad overcoherence of the nuclear and electronic subsystems. That is the electronic and nuclear motion was coupled long after the region of high non-adiabatic coupling (crossing region). The fact that the hops are instant leads to discontinuities and methods need

to be implemented to fix these such as velocity re-scaling. Finally, perhaps the most important shortcoming is that this technique has not been derived from first principles and cannot be guaranteed to work generally. These problems have lead to a number of other techniques being developed. One of these, CTMQC, will be studied in this thesis and is the semi-classical limit of the exact factorisation of the time-dependent Schrödinger equation.

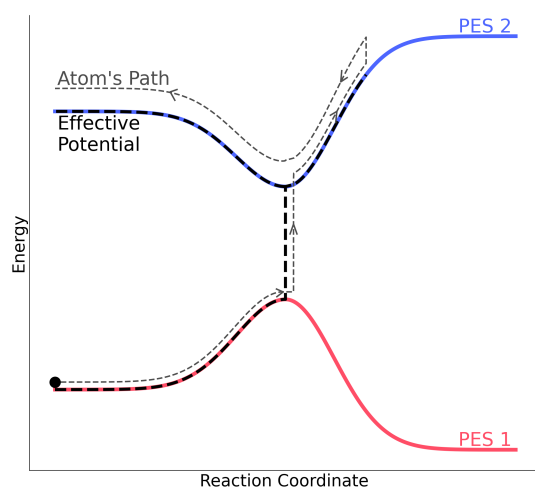


Figure 1.2: An example of a typical Surface Hopping simulation near an avoided crossing. The black lines represent the adiabatic potential energy surface due to the ground (PES 1) and excited (PES 2) state. The red line represents the discontinuous effective potential the nuclei travel on.

1.3 Exact Factorisation

Exact factorisation⁴⁷ involves separating the total molecular wavefunction into a nuclear component and electronic component. Where the electronic component is parametrically dependent on the nuclear coordinates, \mathbf{R} . This is shown below in eq (1.3) where χ is the nuclear wavefunction and Φ is the electronic one.

$$\Psi(\mathbf{R}, \mathbf{r}, t) = \Phi_{\mathbf{R}}(\mathbf{r}, t) \chi(\mathbf{R}, t) \quad (1.3)$$

In the above equation (and throughout this report) I will denote nuclear coordinates and electronic coordinates \mathbf{R} and \mathbf{r} respectively. The nuclear and electronic wavefunctions then obey separate, but coupled, time-dependent Schrödinger equations for spatial and temporal evolution. In this report, I will be focussing on the semi-classical limit of these equations, named Coupled-Trajectory Mixed Quantum-Classical Molecular Dynamics (CTMQC), and give results of a combination of this and the AOM method explained in section ??.

The equations for the evolution of the electronic and nuclear wavefunctions in the exact factorisation⁴⁷ are given below:

$$\hbar \frac{\delta}{\delta t} \Phi_{\mathbf{R}}(\mathbf{r}, t) = (\hat{H}_{BO} + \hat{U}_{en}[\Phi_{\mathbf{R}}, \chi] - \varepsilon(\mathbf{R}, t)) \Phi_{\mathbf{R}}(\mathbf{r}, t) \quad (1.4)$$

$$\hbar \frac{\delta}{\delta t} \chi(\mathbf{R}, t) = \left(\sum_{v=1}^{N_n} \frac{[-\hbar \nabla_v + \mathbf{A}_v(\mathbf{R}, t)]^2}{2M_v} + \varepsilon(\mathbf{R}, t) \right) \chi(\mathbf{R}, t) \quad (1.5)$$

Where \hat{H}_{BO} is the Born-Oppenheimer Hamiltonian, that is $\hat{T}_e + \hat{W}_{ee} + \hat{W}_{nn} + \hat{V}_{en}$. Where \hat{T}_e is the electronic kinetic energy operator, $\hat{W}_{ee/nn}$ is the electron-electron/nuclei-nuclei interaction and V_{en} is the electronic-nuclear potential.

The \hat{U}_{en} is an electronic-nuclear coupling operator (ENCO). This is defined as

$$\hat{U}_{en}[\Phi_{\mathbf{R}}, \chi] = \sum_{v=1}^{N_{nuc}} \frac{1}{M_v} \left[\frac{[-\hbar \nabla_v - \mathbf{A}_v(\mathbf{R}, t)]^2}{2} + \left(\frac{-\hbar \nabla_v \chi}{\chi} + \mathbf{A}_v(\mathbf{R}, t) \right) \left(-\hbar \nabla_v - \mathbf{A}_v(\mathbf{R}, t) \right) \right] \quad (1.6)$$

Where the \mathbf{A}_v is a time-dependent vector potential (TDVP), given by $\langle \Phi_{\mathbf{R}}(t) | -\hbar \nabla_v \Phi_{\mathbf{R}} \rangle_{\mathbf{r}}$ and M_v is the mass of nuclei v . Finally $\epsilon(\mathbf{R}, t)$ is a time-dependent scalar potential energy surface (TDPES), given by $\langle \Phi_{\mathbf{R}}(t) | \hat{H}_{BO} + \hat{U}_{en}^{coup} - \hbar \frac{\delta}{\delta t} | \Phi_{\mathbf{R}}(t) \rangle_{\mathbf{r}}$.

The effects of the TDPES, TDVP and the ENCO have been investigated in multiple works^{1,48–51}. The TDPES and TDVP are both responsible for the evolution of the system⁴⁸. The TDPES provides exact classical forces on the nuclei. In fact, an alternative independent-trajectory semi-classical scheme has been investigated using these exact forces¹. This found the TDPES is responsible for the splitting of the nuclear wavepacket in regions of high non-adiabaticity by taking the shape of a step function between the 2 adiabatic potentials. This is demonstrated in figure

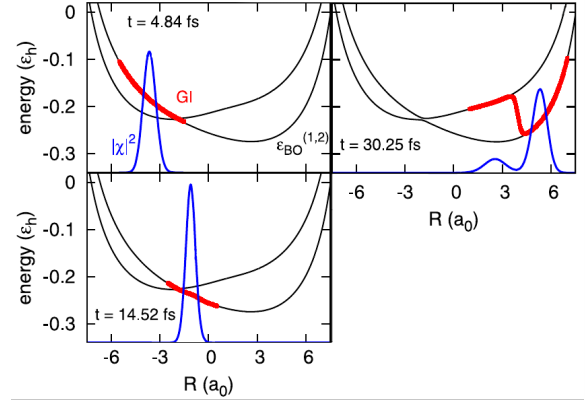


Figure 1.3: A demonstration of how the TDPES can cause the splitting of the nuclear wavepacket in non-adiabatic regions. The red line represents the TDPES and the blue is the nuclear density. Figure adapted from Agostini, 15¹

1.3, which was adapted from an image in Agostini, 15⁴⁸.

Finally the electronic-nuclear coupling operator (ENCO) is responsible for other non-adiabatic effects in the system such as electronic nonadiabatic transitions and decoherence⁴⁸.

1.4 Approximations leading to CTMQC

Starting from the exact factorisation equations, 6 approximations have been made to derive the CTMQC equations. These are discussed in detail in Ref.². In the interest of completeness I have summarised them below.

1.4.1 Classical Nuclei

Techniques that include nuclear quantum effects (NQE)s; such as multiple spawning³¹, ring-polymer surface hopping⁵² and nonadiabatic Bohmian dynamics^{53,54} although extremely accurate, cannot be applied to hundreds or thousands of molecules, due to their high computational cost. Further, in many systems of interest NQEs are negligible, especially at room temperature. For this reason the classical limit of the nuclear Schrödinger equation (1.5) is taken when deriving the CTMQC equations.

1.4.2 Neglect the ENCO in the TD PES

The electron-nuclei coupling operator is omitted in the expression for the time-dependent potential energy surface. This is justified as the first term $([-\hbar\nabla_{\mathbf{v}} - \mathbf{A}_{\mathbf{v}}(\mathbf{R}, t)]^2)$ contains a second order derivative which is expensive to calculate and has a negligible effect compared to the second term in the ENCO⁵⁵. However, the rest of the ENCO is equal to zero when averaged over $\Phi_{\mathbf{R}}(\mathbf{r}, t)$ so it does not contribute to the TD PES.

1.4.3 Derivative of the Adiabatic Coefficients

The derivative of the adiabatic coefficients appears in the electronic evolution equations. However, we can re-write the derivative of the adiabatic coefficients in terms of their modulus and phase:

$$\nabla_{\mathbf{v}} C_l^{(I)}(t) = \left[\underbrace{\frac{\nabla_{\mathbf{v}} |C_l^{(I)}(t)|}{|C_l^{(I)}(t)|}}_{\text{(Term 1)}} + \underbrace{\frac{i}{\hbar} \nabla_{\mathbf{v}} \gamma_l^{(I)}(t)}_{\text{(Term 2)}} \right] C_l^{(I)}(t) \quad (1.7)$$

It has been found that the first term is negligible compared to the second^{1,49,50} so it doesn't need to be calculated and we can remove it. It was also assumed that the NACVs are localised in space meaning that, after some algebra, the spatial derivative of the adiabatic coefficient can be written as:

$$\nabla_{\mathbf{v}} C_l^{(I)}(t) = \frac{i}{\hbar} \nabla_{\mathbf{v}} \gamma_l^{(I)}(t) C_l^{(I)}(t) = -\frac{i}{\hbar} \int^t dt' \nabla_{\mathbf{v}} \epsilon_l^{(I)} C_l^{(I)}(t) = -\frac{i}{\hbar} \mathbf{f}_l^{(I)} C_l^{(I)}(t) \quad (1.8)$$

Where $\epsilon_l^{(I)}$ is the energy of the l^{th} adiabatic potential energy surface for trajectory I, $C_l^{(I)}$ is the adiabatic expansion coefficient for state l and trajectory I. The $\mathbf{f}_l^{(I)}$ is the time-integrated adiabatic force (adiabatic momentum).

1.4.4 Gaussian Nuclear Wavepackets

In order to calculate the quantum momentum -the new term in CTMQC. Knowledge of the nuclear distribution is needed. However, as we treat the nuclei as point particles we need to re-construct the nuclear density from the atomic positions. This is done by smoothing out the atomic positions by placing a gaussian of width σ centered on each atomic position and combining these gaussians to produce the final nuclear density. This introduces an empirical parameter (σ) which will be discussed later in this thesis. It should be noted, the nuclei are still propagated classically, the width parameter is only used in the calculation of the quantum momentum.

1.4.5 Separating the Effects of Decoherence and NACVs

So as to not introduce any population transfer (due to the quantum momentum) when the NACV is zero a fifth approximation has been introduced. Namely the quantum momentum depends on pairs of states - l,k . This enables the separation of the ‘competing’ effects of the NACV and the Quantum Momentum.

1.5 The CTMQC equations

1.5.1 Adiabatic Basis

The equations for the propagation of the classical nuclei and the expansion coefficients in the CTMQC framework in the adiabatic basis are given below:

$$\begin{aligned} \dot{\mathbf{P}}_v^{(I)} = & \underbrace{-\sum_k |C_k^{(I)}|^2 \nabla_v \epsilon_k^{(I)} - \sum_{k,l} C_l^{(I)} C_k^{*(I)} \left(\epsilon_k^{(I)} - \epsilon_l^{(I)} \right)}_{\text{Ehrenfest}} \\ & - \underbrace{\sum_{l,k} |C_l^{(I)}|^2 \left(\sum_{v'=1}^{N_n} \frac{2}{\hbar M_{v'}} \mathcal{Q}_{lk,v}^{(I)} \cdot \mathbf{f}_{l,v}^{(I)} \right) \left[|C_k^{(I)}|^2 \mathbf{f}_{k,v}^{(I)} - \mathbf{f}_{l,v}^{(I)} \right]}_{\text{Quantum Momentum}} \end{aligned} \quad (1.9)$$

$$\begin{aligned}
\dot{C}_l^{(I)} = & \overbrace{-\frac{i}{\hbar} \epsilon_l^{(I)} C_l - \sum_k C_k^{(I)} d_{lk}^{ad(I)}}^{\text{Ehrenfest}} \\
& \underbrace{- \sum_{v=1}^{N_n} \sum_k \frac{\mathcal{Q}_{lk,v}^{(I)}}{\hbar M_v} \cdot [\mathbf{f}_{k,v}^{(I)} - \mathbf{f}_{l,v}^{(I)}] |C_k^{(I)}|^2 C_l^{(I)}}_{\text{Quantum Momentum}}
\end{aligned} \tag{1.10}$$

Where the ϵ_k term is the potential energy on the k^{th} potential energy surface. C_l is the adiabatic expansion coefficient corresponding to the l^{th} state. The sum over k and l indicates a sum over all states, the (I) superscript is a replica index and the v is an atom index. M_v is the nuclear mass and $d_{lk}^{ad(I)}$ represents the non-adiabatic coupling element (in the adiabatic basis) between adiabatic states l and k . The 2 new terms in this scheme not seen in other NAMD methods are the $\mathcal{Q}_{lk,v}^{(I)}$ and the $\mathbf{f}_{k,v}^{(I)}$. These are the quantum momentum and the adiabatic momentum. The adiabatic momentum term is defined in equation (1.8) this keeps a record of the previous forces on each adiabatic state in the system. The quantum momentum term couples the trajectories together (making this a coupled-trajectory scheme). Together the history dependent force and quantum momentum are responsible for the decoherence in the ‘Quantum Momentum’ parts of the above equations³. Notably, although these equations have been derived from the exact factorisation equations separately from Ehrenfest they do contain the Ehrenfest equations within them (marked ‘Ehrenfest’). This scheme can therefore be seen as an Ehrenfest scheme with a correction that captures branching of the nuclear wavefunction and decoherence within it.

We can also see in equation (1.10) if we are in a pure adiabatic state i.e. all population on a single adiabatic state, there is no contribution from the quantum momentum part of the equations. In this scenario the evolution equations become simply Ehrenfest equations. For example, if all the population is localised on a single adiabatic state then the term $|C_k^{(I)}|^2 C_l$ is only non-zero when $l = k$. However, when $l = k$, the term $[\mathbf{f}_{k,v}^{(I)} - \mathbf{f}_{l,v}^{(I)}]$ is zero as $\mathbf{f}_{k,v}^{(I)} = \mathbf{f}_{l,v}^{(I)}$. Therefore, the quantum momentum term can be seen to only kick in when there is a mixing of adiabatic states. In the adiabatic formulation of these equations it is the adiabatic NACV $\mathbf{d}_{lk,v}^{ad(I)}$ that is responsible for the initial mixing of the

populations from pure adiabatic states.

1.6 Calculating the Quantum Momentum

The technique for calculating the quantum momentum term is outlined in detail in the SI of min, 17⁵⁶. The original equations given in Agostini, 16² present a quantum momentum term without state indices (l,k). This, due to approximations made in the derivation of CTMQC, results in population transfer even when the non-adiabatic couplings between states are zero. Therefore, Agostini et al enforced this condition with the pair-wise state dependence on the quantum momentum. The quantum momentum is defined in equation (1.11) as:

$$\mathcal{Q}_v^{(I)} = \frac{-\hbar \nabla_v |\chi^{(I)}|}{|\chi^{(I)}|} \frac{-\hbar \nabla_v |\chi^{(I)}|^2}{2|\chi^{(I)}|^2} \quad (1.11)$$

In order to reconstruct the nuclear density, Gaussian distributions are used as in equation (1.12) below:

$$|\chi^{(I)}(t)|^2 = \frac{1}{N_{tr}} \sum_{J=1}^{N_{tr}} \prod_{v=1}^{N_n} g_{\sigma_v^{(J)}(t)} \left(\mathbf{R}_v^{(I)}(t) - \mathbf{R}_v^{(J)}(t) \right) \quad (1.12)$$

Where, N_{tr} is the number of trajectories, N_n is the number of atoms, $\sigma_v^{(J)}(t)$ is a time-dependent width parameter for each gaussian g and $\mathbf{R}_v^{(J)}$ represents the atomic position of atom \mathbf{v} on trajectory J .

This results in a linear expression for the quantum momentum. The full details of the derivation are given in the supplementary information of Min, 17⁵⁶. The resulting linear expression for the quantum momentum is given below:

$$\mathcal{Q}_{lk,v}^{(I)} = \alpha_v^{(I)} \mathbf{R}_v^{(I)} - \mathbf{R}_{lk,v} \quad (1.13)$$

Where $\mathbf{R}_v^{(I)}$ are the nuclear coordinates on trajectory I on atom \mathbf{v} . The $\alpha_v^{(I)}$ term is a weighted average over trajectories of the product of the gaussian's assigned to each atomic

coordinate, i.e:

$$\alpha_v^{(I)} = \sum_J \frac{\hbar \prod_{v'} g_{\sigma_{v'}^{(J)}(t)} \left(\mathbf{R}_{v'}^{(I)}(t) - \mathbf{R}_{v'}^{(J)}(t) \right)}{2 \sigma_v^{(J)}(t)^2 \sum_K^{N_{tr}} \prod_{v'} g_{\sigma_{v'}^{(K)}(t)} \left(\mathbf{R}_{v'}^{(I)}(t) - \mathbf{R}_{v'}^{(K)}(t) \right)} \quad (1.14)$$

Along with the $\mathbf{R}_{lk,v}$ term the $\alpha_v^{(I)}$ performs the job of coupling the trajectories together. The $\mathbf{R}_{lk,v}$ term also given in the SI of Min, 17⁵⁶ is defined for each Cartesian dimension as:

$$R_{lk,v} = \sum_I^{N_{tr}} R_v^{(I)}(t) \alpha_v^{(I)}(t) \frac{|C_k^{(I)}(t)|^2 |C_l^{(I)}(t)|^2 \left(f_{k,v}^{(I)}(t) - f_{l,v}^{(I)}(t) \right)}{\sum_J |C_k^{(J)}(t)|^2 |C_l^{(J)}(t)|^2 \left(f_{k,v}^{(J)}(t) - f_{l,v}^{(J)}(t) \right)} \quad (1.15)$$

Where the bold notation for vectors has been replaced by normal font indicating that this applies to each cartesian dimension independently. Further, in this expression $R_{lk,v}$ is symmetric, $R_{lk} = R_{kl}$ meaning that $Q_{lk} = Q_{kl}$. At first sight, the R_{lk} term seems to be another weighted average. However, this isn't quite the case as the denominator can be negative. This causes equation (1.15) to be very sensitive to errors in the calculation of the denominator of this fraction. Any inaccuracies can lead to the denominator approaching zero faster than the numerator causing large spikes in the quantum momentum term. This will be discussed in greater detail in the following chapters.

Chapter 2

CTMQC applied to the Tully Models

The Tully models, first proposed by John Tully in 1990⁵⁷, are a collection of simple 1 dimensional model systems. They were designed to be simple enough to obtain accurate quantum results to benchmark new nonadiabatic molecular dynamics (NAMD) methods against. Originally there were 3, 1 dimensional, 1 atom models. However, in this work an extra model has been introduced with parameters taken from Gossel, 18³. This is to allow a full comparison of my implementation of CTMQC with the literature. In this chapter my implementation of CTMQC will be tested using these model systems and by comparing my results with those in the literature.

In each of the Tully models the (diabatic) Hamiltonian is a function of nuclear positions and is a 2×2 matrix that takes the form:

$$\hat{H} = \frac{\hat{P}^2}{2M} + \begin{pmatrix} H_{11}(\mathbf{R}) & H_{12}(\mathbf{R}) \\ H_{21}(\mathbf{R}) & H_{22}(\mathbf{R}) \end{pmatrix} \quad (2.1)$$

The nuclear mass has been set to 2000 a.u.. This was set to be very close to the proton's mass of 1836 a.u. so we can expect significant quantum effects that classical theory couldn't replicate. The values of the Hamiltonian matrix elements are set to produce systems that resemble common features in a typical nonadiabatic simulation such as avoided crossings and regions of extended coupling. The parameters used in each systems' Hamiltonian were taken from Gossel, 18³ in order to compare the 2 implementations. These can be found in appendix A.

In order to propagate dynamics in the adiabatic basis we need to calculate various quantities from the hamiltonian at each timestep. These are, for Ehrenfest, the (adiabatic) nonadiabatic coupling vector ($\mathbf{d}_{lk}^{(I)}$) and the adiabatic energies ($E_l^{(I)}$). In the full CTMQC simulations we must also calculate the adiabatic momentum term $\mathbf{f}_l^{(I)}$ from the Hamiltonian. The adiabatic energies are the eigenvalues of the Hamiltonian. The adiabatic NACV can be calculated via a finite difference method and equation (2.2) below.

$$\mathbf{d}_{lk}^{(I)} = \langle \psi_l^{(I)} | \nabla \psi_k^{(I)} \rangle \quad (2.2)$$

Where $\psi_l^{(I)}$ is the adiabatic electronic basis function for adiabatic state l. This is given by the eigenvector of the Hamiltonian, on replica I, corresponding to state l. Illustrations of these 2 properties can be found below in fig 2.1 for each of the 4 models systems.

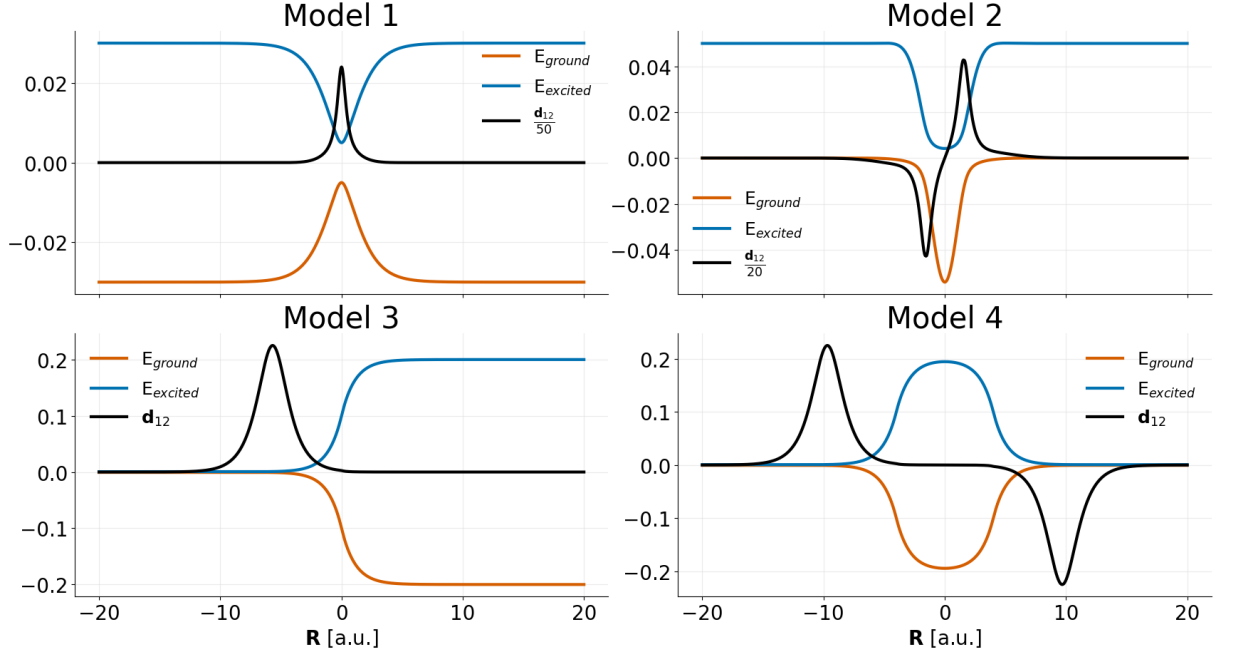


Figure 2.1: Adiabatic potential energy surfaces (orange and blue) and element 1, 2 of the nonadiabatic coupling vector (black) for the 4 model systems. For parameters see appendix A.

In order to initialise the simulations coordinates and velocities were sampled from the Wigner phase-space distribution of a gaussian nuclear wavepackets given by equation (2.3). A derivation of this can be found in appendix B. The nuclear positions/velocities were then propagated using a velocity verlet algorithm and the adiabatic expansion coefficients were propagated using a 4th order Runge-Kutta method.

$$\chi(R,0) = \frac{1}{(\pi\mu^2)^{\frac{1}{4}}} e^{-\frac{(R-R_0)^2}{2\mu^2} + ik_0(R-R_0)} \quad (2.3)$$

The adiabatic coefficients were initialised purely on the ground state and the initial width of the nuclear wavepacket was set to $\mu = \sqrt{2}$ bohr. 2 values of initial momenta k_0 were chosen for each model, 1 low value and another higher one. Full details of all input parameters can be found in appendix A. I have implemented a serial version of CTMQC acting on Tully’s toy model systems and real molecular systems using couplings derived from the analytic overlap method⁵⁸ within the software package CP2K⁵⁹ and for Tully’s model systems as standalone python code. These are accessible publicly via github repositories at: github.com/95ellismle.

2.1 Testing My Implementation

The motivation behind implementing CTMQC for the Tully models was to serve as a verifiable base for later extensions, such as integrating CTMQC within the fragment-orbital based (FOB)⁶⁰ framework which will be discussed in a later chapter[?]. Using such simple systems will also help to clarify how each new parameter works and make testing and debugging easier. As well as many numerical tests on individual terms in the equations, I have implemented some physical tests on the overall system dynamics. In this section, I will outline the key tests I have performed on both the Ehrenfest and full CTMQC parts of the equations. These are: ...

2.1.1 Comparisons To Literature

There have been 2 papers published applying CTMQC to the Tully models^{2,3} and both contain results for the 4 Tully models shown in fig 2.1. The results contain data on the (ground state) adiabatic populations and a coherence indicator as shown in equation (2.4) for 16 different simulations (a low and high initial momentum simulation of Models 1, 2, 3 and 4).

$$|\rho_{12}(t)|^2 = \frac{1}{N_{tr}} \sum_{I=1}^{N_{tr}} |C_1^{(I)}(t)|^2 |C_2^{(I)}(t)|^2 \quad (2.4)$$

In order to compare to results in the literature the same setup had to be used. In this case this meant sampling individual trajectory initial conditions (positions and momenta) from a Wigner distribution with a mean position and momenta given in appendix A. The wavefunction was initialised purely on the ground state and the same integrator was used for the nuclear and electronic propagation (velocity verlet and RK4 respectively).

2.1.2 Ehrenfest

My results as well as the relevant data taken from Agostini, 16 and Gossel, 18^{2,3} are shown in figure 2.2 for Ehrenfest dynamics. This is equivalent to full CTMQC dynamics where the quantum momentum term is set to 0. Hence, we can test most parts of the code (i.e. Runge-Kutta propagation, velocity verlet, inputs, force calculations etc...) while ignoring the new quantum momentum and accumulated adiabatic force terms.

The results in figure 2.2 show that both the adiabatic populations and coherence indicator give exactly the same results as in the literature, within reasonable error. Any deviations of results come from either a slightly different initial sampling of positions (sampled from a Wigner distribution) or small errors in retrieving data from the graphs in each paper. For example, in the case of the high initial momentum simulation of model 4 all 3 results show some differences though the trend is very similar. This is true also in the Model 2 results where the Agostini, 16 populations show some transient oscillations before settling onto the same equilibrium population. This may be due to a

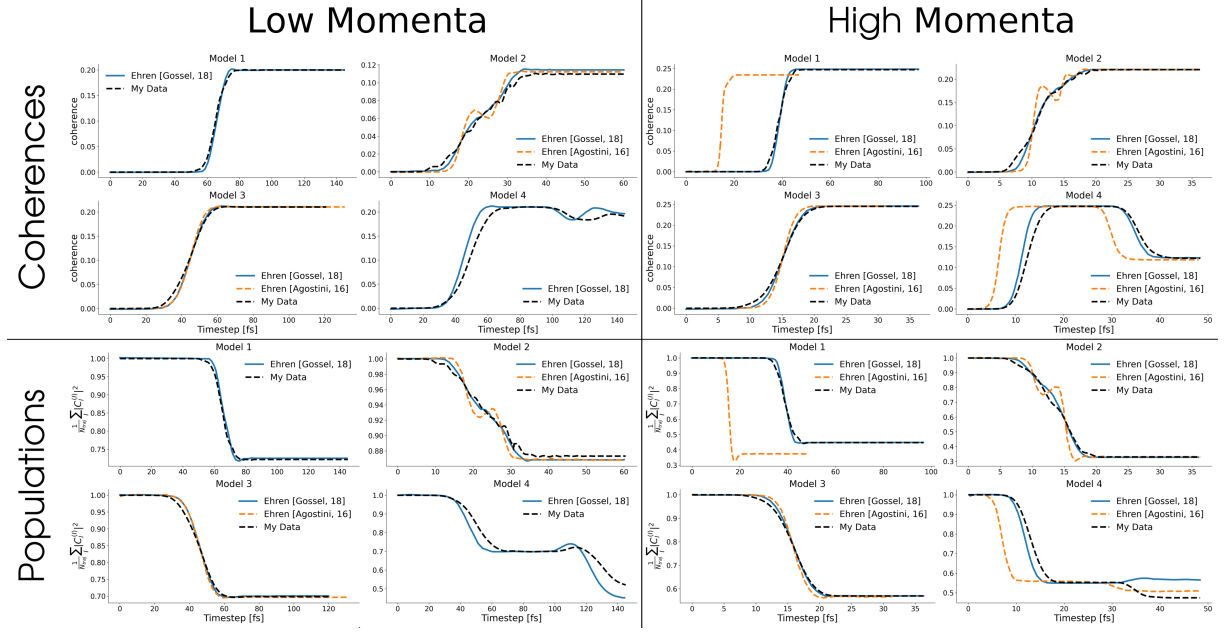


Figure 2.2: A comparison of my implementation of Ehrenfest (for 4 model Hamiltonians) and results from the literature. The black dashed lines show my data (ground state ad pops), the orange dashed lines are data from Agostini, 16² and the blue solid lines are from Gossel, 18³. The figures are labelled with their model number, whether the initial momentum was high or low and whether the populations or coherence indicator was plotted.

smaller spread of positions being used in the initial sample leading to similar oscillations that aren't smoothed out in the averaging over all trajectories. There are also a couple of models that start at a slightly different initial mean position in Frederica, 16 thus they hit the nonadiabatic crossing region sooner. These are model 1 and 4 for the high momentum case.

Although not all results are exactly the same, I believe the populations agree well enough within a reasonable error to serve as a confirmation of my implementation.

2.1.3 CTMQC

To test the full CTMQC equations I now turn on the quantum momentum ($\mathcal{Q}_{lk,v}^{(I)}$) and accumulated adiabatic force ($\mathbf{f}_{l,v}^{(I)}$) terms. These provide the extra decoherence that is missing in the standard Ehrenfest representation and allow populations of individual trajectories to collapse onto a single adiabatic state. Without these terms (e.g. in Ehrenfest dynamics) all trajectories follow the same mean potential energy surface and detailed

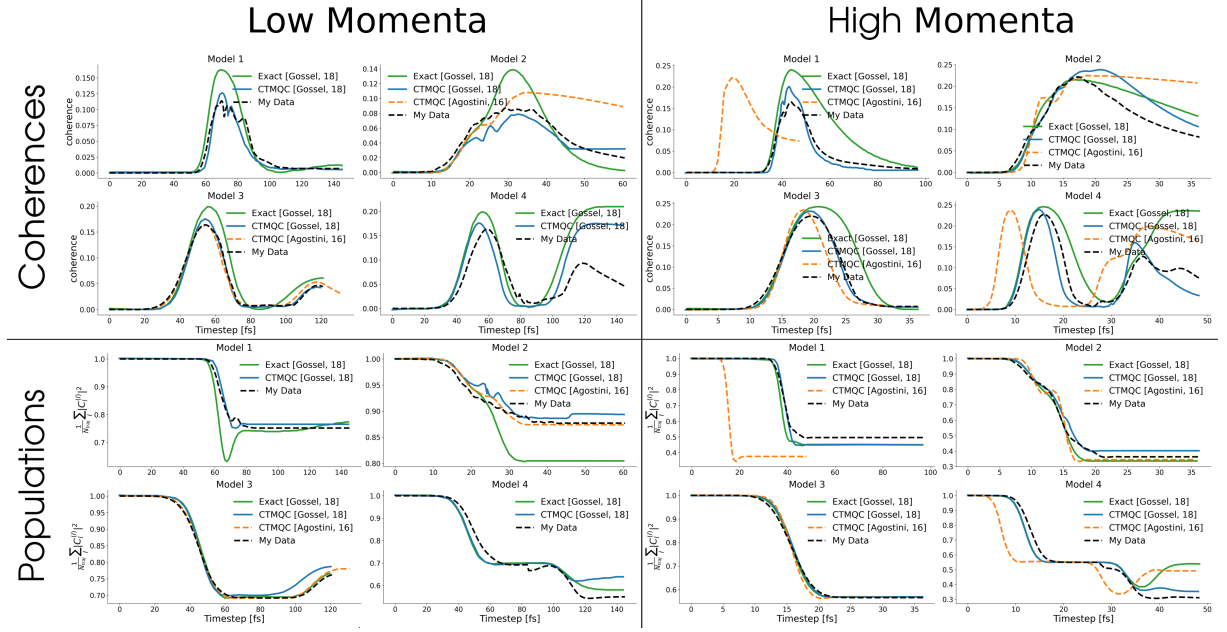


Figure 2.3: A comparison of my implementation of full CTMQC (for 4 model Hamiltonians) and results from the literature. The black dashed lines show my CTMQC data (ground state ad pops), the orange dashed lines are data from Agostini, 16² and the blue solid lines are from Gossel, 18³. The solid green line shows data from exact quantum mechanical simulations given in Gossel, 18. The figures are labelled with their model number, whether the initial momentum was high or low and whether the populations or coherence indicator was plotted.

balance is not conserved.

The results for my implementation are given in figure 2.3. This time, unlike in the Ehrenfest code, we see some major discrepancies between the 3 results. These cannot solely be explained as small errors from slightly different sampling of initial positions. We can see that the errors mainly appear in the coherence indicator, looking at the bottom row in figure 2.3 it appears that both the Agostini and Gossel results match mine (in dashed black line) very closely. The largest difference is seen in model 4, high momentum where the Gossel data and mine follow a similar trend and the Agostini data follows the exact curve more closely. However, looking at the coherence indicators in the above row we see a different story. My data tends to follow the Gossel data fairly closely, while the Agostini data follows a different pattern. This is due to differing parameters being used to calculate the quantum momentum term.

To calculate the quantum momentum one must take the spatial derivative of the nuclear density. However, the nuclei are classical and represented by a point. In order to calculate the nuclear density the procedure outlined in the supplementary information of Min, 17⁵⁶ was to smear out the nuclear density by describing each classical atom with a gaussian distribution of width σ and mean $\mathbf{R}_v^{(I)}(t)$ (i.e. the atomic position). The method for determining the parameter σ has not been outlined therefore it is very hard to develop a method to exactly reproduce the results found in the 2 CTMQC papers. In figure 2.3 a constant sigma of $\sigma = 0.35$ bohr was taken to closely match the Gossel, 18 data. The fact that the curves match in many cases almost exactly makes me think this was the method employed in Gossel, 18 too. It also serves as a confirmation of the full implementation of CTMQC.

2.1.4 Norm Conservation

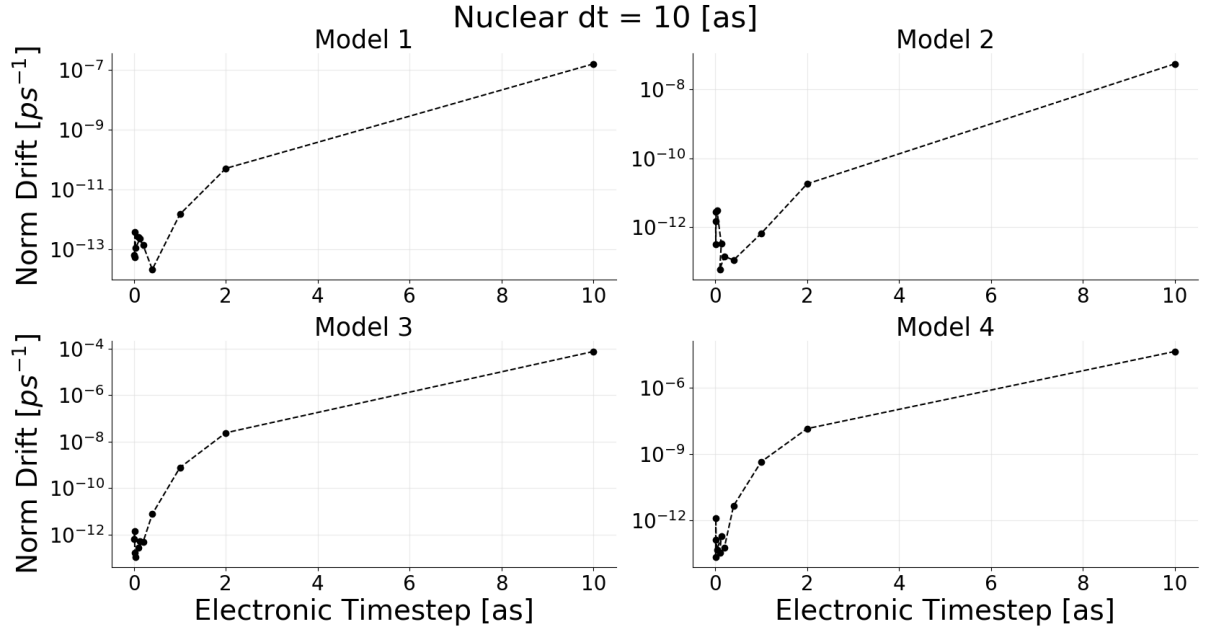


Figure 2.4: The norm conservation averaged over all replicas for Ehrenfest simulations with various electronic timesteps for each Tully model using a initial high momenta.

In appendix E, it is shown that the norm of the adiabatic expansion coefficients should be conserved throughout the simulation. In order to test this various simulations were carried out with various size electronic timesteps (i.e. the timestep used to propagate the electronic subsystem). As can be seen in figure 2.4, the norm of the wavefunction

is conserved within numerical error (10^{-12}) when using a sufficiently small timestep in every Tully model. However, when we now use the full CTMQC equation we see a very different picture.

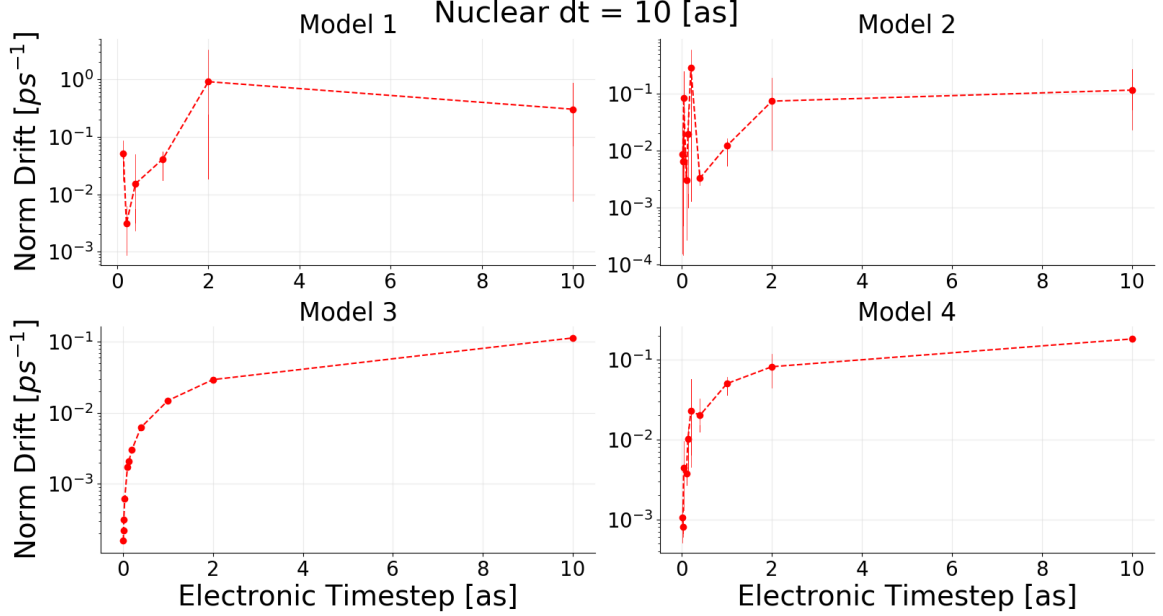


Figure 2.5: The norm conservation when using standard CTMQC as outlined in the literature for each of the Tully models. These simulations were ran with a high initial momentum. The red markers show data points and vertical bars show error bars associated with each point.

In figure 2.5, we can see that only in Model 3 we see a similar trend as in Ehrenfest for the norm conservation -i.e. a decreasing electronic timestep gives a rapidly decreasing norm drift. In models 1 and 2 we see that the norm drift doesn't get much better as we decrease the timestep and there are large error bars associated with each data point. In model 4 this is less pronounced but is still clearly effected. This is due to an instability in the way the quantum momentum term ($\mathcal{Q}_{lk,v}^{(I)}$) is calculated.

The calculation of the quantum momentum is discussed in detail in Min, 17⁵⁶ and outlined in the introduction to the thesis in section 1.6. As mentioned in that section, the denominator in the expression for $\mathbf{R}_{lk,v}$ may be positive or negative and when it switches between the 2 it can approach zero very closely. If this denominator approaches zero more quickly than the numerator then we can see large spikes in the $\mathbf{R}_{lk,v}$ term which can

lead to large norm drifts.

2.1.4.1 Quantum Momentum Instabilities

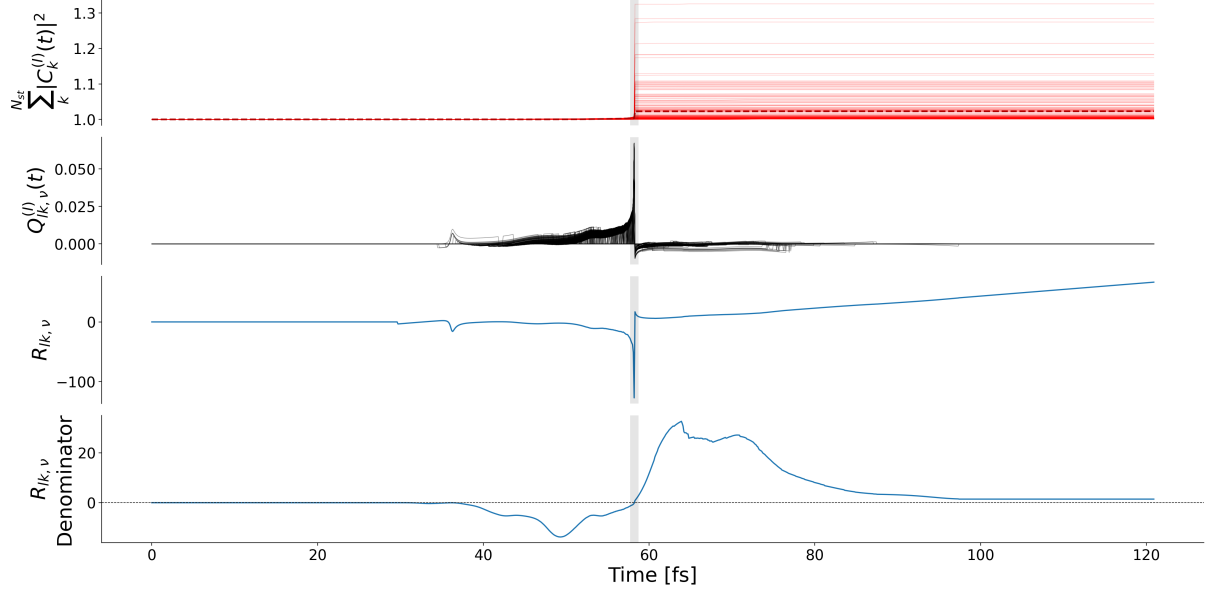


Figure 2.6: As the denominator of the $\mathbf{R}_{lk,v}$ term approaches zero (bottom panel) the full $\mathbf{R}_{lk,v}$ term (2nd to bottom panel) can approach infinity which propagates through the $\mathcal{Q}_{lk,v}^{(l)}$ term (2nd to top panel) causing discontinuities and norm drift in the populations (top panel). The grey vertical bar denotes the region the denominator approaches 0.

As we can see in figure 2.6, as the denominator of the $\mathbf{R}_{lk,v}$ term approaches 0 the full $\mathbf{R}_{lk,v}$ term may spike causing a discontinuity in the populations. The reason this only occurs in Models 1, 2 and 4 is due to the fact that the difference in the adiabatic momenta terms $(\mathbf{f}_{l,v}^{(l)} - \mathbf{f}_{k,v}^{(l)})$ doesn't cross 0 in Model 3. In order to correct for this I have investigated a number of corrections to the calculation of the quantum momentum. These depend on the detection of the spikes/divergences in the $\mathbf{R}_{lk,v}$ term and then the appropriate treatment of them. In order to detect the divergences a simple threshold on the $|\frac{\delta}{\delta t} \mathbf{R}_{lk,v}|$ is applied when the denominator of the $\mathbf{R}_{lk,v}$ is sufficiently close to 0. For example, if the absolute time-derivative of the $\mathbf{R}_{lk,v}$ term is larger than a value (say 5) and the bottom of the fraction in equation (1.15) is within 0.1 of 0 then we assume the $\mathbf{R}_{lk,v}$ term is diverging and the simulation code then uses a different method of propagating the electronic coefficients.

The alternative propagation methods I have investigated are:

1. Use Ehrenfest Dynamics (set $\mathcal{Q}_{lk,v}$ term to 0).
2. Extrapolate the value of $\mathbf{R}_{lk,v}$ from values before the divergence (see appendix C.1).
3. Switch to using the alternative intercept $\mathbf{R}_{0,v}^{(I)}$ (see appendix C.2).

of these 3 methods, method 3 was the most successful in reducing the norm drift in the Tully Models as can be seen in figure 2.7. In figure 2.7 we see the norm drift results after

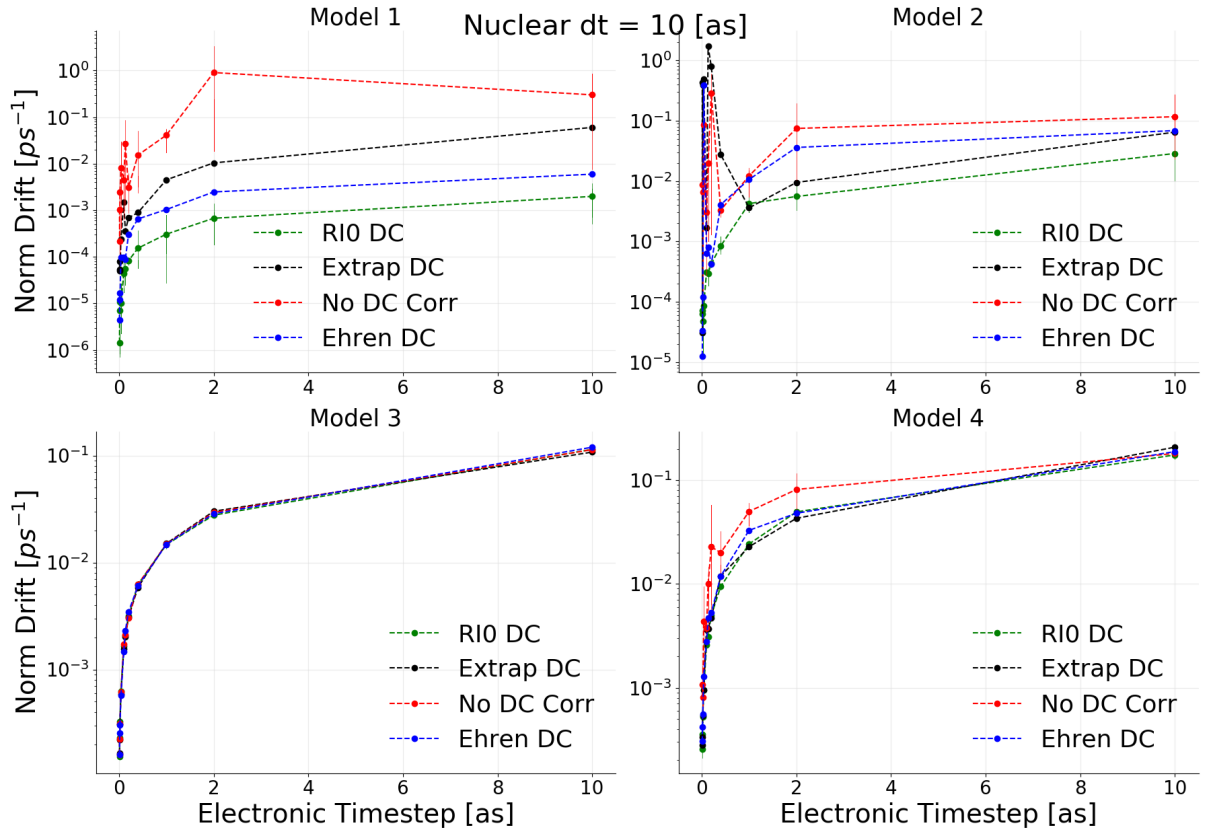


Figure 2.7: Norm conservation in CTMQC after applying a divergence correction to the $\mathbf{R}_{lk,v}$ term. RI0 refers to method 3, Extrap DC refers to method 2 and Ehren DC refers to method 1. No DC Corr shows the population norm without any corrections applied.

the 3 $\mathbf{R}_{lk,v}$ correction methods have been applied. The red curve shows the original data (as in figure 2.5) with its large divergences in the norm drift. The green curve shows the alternative intercept method, the blue curve shows the effect of switching to Ehrenfest during the $\mathcal{Q}_{lk,v}^{(I)}$ spikes and the black shows a method that involved extrapolating the $\mathbf{R}_{lk,v}$ value from data before the spike began. We can see clearly all 3 methods improve

the norm drift, though using the alternative intercept seems to help the most. Model 3 is not affected as we do not see these divergences in the $\mathbf{R}_{lk,v}$ due to the denominator in this particular model never crossing from positive to negative (through zero). It is important to note that in each of the models with the divergence correction applied all models exhibit the expected trend of decreasing the time-step improves norm conservation. However, the norm conservation in all 4 models is still significantly higher (~ 7 -8 orders of magnitude) higher than that of Ehrenfest. I think this is due to the product of the adiabatic populations, $|C_l^{(I)}|^2 |C_k^{(I)}|^2$, being used in the calculation of the quantum momentum which can be a more quickly varying quantity than just the adiabatic populations alone.

2.1.5 Time Derivative of Trajectory-Sum of Adiabatic Populations

...

2.1.6 Energy Conservation

...

Appendix A

Tully Model Paramters

A.1 Model 1 -Single Avoided Crossing

Hamiltonian Paramters:

$$H_{11}(\mathbf{R}) = A \tanh(B\mathbf{R})$$

$$H_{12}(\mathbf{R}) = Ce^{-D\mathbf{R}^2}$$

$$H_{21}(\mathbf{R}) = H_{12}(\mathbf{R})$$

$$H_{22}(\mathbf{R}) = -H_{11}(\mathbf{R})$$

Where A = 0.03, B = 0.4, C = 0.005 and D = 0.3

Quantity	Value	Unit
Initial Position	-20	a.u.
Initial Velocities	15.0, 25.0	a.u.
Initial Adiab Pop	ground state	-
Simulation Time	6000, 4000	a.u.
$\sigma_v^{(I)}$	0.5	a.u.
M (σ constant)	40	-
$\Delta t_{\text{nuclear}}$	0.1	fs
$\Delta t_{\text{electronic}}$	0.01	fs
$\frac{\delta \mathbf{R}_{lk,v}^{(I)}}{\delta t}$ threshold	0.15	a.u.
N_{rep}	200	-

A.2 Model 2 -Dual Avoided Crossing

	Quantity	Value	Unit
Hamiltonian Paramters:	Initial Position	-8	a.u.
	Initial Velocities	16.0, 30.0	a.u.
$H_{11}(\mathbf{R}) = 0$	Initial Adiab Pop	ground state	-
$H_{12}(\mathbf{R}) = Ce^{-D\mathbf{R}^2}$	Simulation Time	2500, 1500	a.u.
$H_{21}(\mathbf{R}) = H_{12}(\mathbf{R})$	$\sigma_v^{(I)}$	0.5	a.u.
$H_{22}(\mathbf{R}) = -Ae^{-B\mathbf{R}^2} + E$	M (σ constant)	40	-
	$\Delta t_{\text{nuclear}}$	0.1	fs
Where A = 0.1, B = 0.28, C = 0.015, D =	$\Delta t_{\text{electronic}}$	0.01	fs
0.06 and E = 0.05	$\frac{\delta \mathbf{R}_{lk,v}^{(I)}}{\delta t}$ threshold	0.15	a.u.
	N_{rep}	200	-

A.3 Model 3 -Extended Coupling

	Quantity	Value	Unit
Hamiltonian Paramters:	Initial Position	-15	a.u.
	Initial Velocities	10, 30	a.u.
$H_{11}(\mathbf{R}) = A$	Initial Adiab Pop	ground state	-
$H_{12}(\mathbf{R}) = \begin{cases} Be^{C\mathbf{R}}, & R \leq 0 \\ B(2 - e^{-C\mathbf{R}}), & R > 0 \end{cases}$	Simulation Time	5000, 1500	a.u.
$H_{21}(\mathbf{R}) = H_{12}(\mathbf{R})$	$\sigma_v^{(I)}$	0.5	a.u.
$H_{22}(\mathbf{R}) = -H_{11}(\mathbf{R})$	M (σ constant)	40	-
	$\Delta t_{\text{nuclear}}$	0.1	fs
	$\Delta t_{\text{electronic}}$	0.01	fs
Where A = 6×10^{-4} , B = 0.1 and C = 0.9	$\frac{\delta \mathbf{R}_{lk,v}^{(I)}}{\delta t}$ threshold	0.15	a.u.
	N_{rep}	200	-

A.4 Model 4 -Dual Arch

Hamiltonian Paramters:

$$H_{11}(\mathbf{R}) = A$$

$$H_{12}(\mathbf{R}) = \begin{cases} B \left[-e^{C(\mathbf{R}-D)} + e^{C(\mathbf{R}+D)} \right] & R \leq -D \\ B \left[e^{-C(\mathbf{R}-D)} - e^{-C(\mathbf{R}+D)} \right] & R \geq D \\ B \left[2 - e^{C(\mathbf{R}-D)} - e^{-C(\mathbf{R}+D)} \right] & -D < R < D \end{cases}$$

$$H_{21}(\mathbf{R}) = H_{12}(\mathbf{R})$$

$$H_{22}(\mathbf{R}) = -H_{11}(\mathbf{R})$$

Where $A = 6 \times 10^{-4}$, $B = 0.1$ and $C = 0.9$

Quantity	Value	Unit
Initial Position	-20	a.u.
Initial Velocities	10, 40	a.u.
Initial Adiab Pop	ground state	-
Simulation Time	6000, 2000	a.u.
$\sigma_v^{(I)}$	0.5	a.u.
M (σ constant)	40	-
$\Delta t_{\text{nuclear}}$	0.1	fs
$\Delta t_{\text{electronic}}$	0.01	fs
$\frac{\delta \mathbf{R}_{lk,v}^{(I)}}{\delta t}$ threshold	0.15	a.u.
N_{rep}	200	-

Appendix B

Wigner Distribution Derivation

The nuclear wavepacket (at time 0) is given by:

$$\chi(R) = \frac{1}{(\pi\mu^2)^{\frac{1}{4}}} e^{-\frac{(R-R_0)^2}{2\mu^2} + ik_0(R-R_0)} \quad (\text{B.1})$$

The Wigner quassprobability function for momentum and position (p, R) is given by:

$$W(p, R) = \frac{1}{\pi\hbar} \int_{-\infty}^{\infty} \chi^*(R+y) \chi(R-y) e^{\frac{2ipy}{\hbar}} dy \quad (\text{B.2})$$

However, both Ehrenfest and CTMQC require atomic positions as input so we must extract the position and velocity probability densities from this. We get these from the marginal integrals of the Wigner distribution i.e.

$$|f(R)|^2 = \int_{-\infty}^{\infty} W(R, p) dp \quad (\text{B.3})$$

$$|f(p)|^2 = \int_{-\infty}^{\infty} W(R, p) dR \quad (\text{B.4})$$

In order to calculate these marignal integrals we must first crunch through the maths of equation (B.2). Substituting eq (B.1) into (B.2):

$$W(p, R) = \frac{1}{\pi\hbar} \int_{-\infty}^{\infty} \frac{1}{\mu\sqrt{\pi}} e^{-\frac{(R+y-R_0)^2}{2\mu^2} - 2ik_0y - \frac{(R-y-R_0)^2}{2\mu^2}} e^{\frac{2ipy}{\hbar}} dy \quad (\text{B.5})$$

Simplifying the 2 quadratic equations (equation (B.5)) we get:

$$W(p, R) = \frac{1}{\pi\hbar} \int_{-\infty}^{\infty} \frac{1}{\mu\sqrt{\pi}} e^{-\mu^{-2}(y^2 - 2ik_0 y \mu^2 + (R - R_0)^2)} e^{\frac{2ipy}{\hbar}} dy \quad (\text{B.6})$$

We can now take the expressions not dependant on y outside of the integral and combine the exponents.

$$W(p, R) = \frac{1}{\pi\sqrt{\pi}\mu\hbar} e^{-\frac{(R-R_0)^2}{\mu^2}} \int_{-\infty}^{\infty} e^{-\frac{y^2 + 2iy\mu^2(\frac{p}{\hbar} - k_0)}{\mu^2}} dy \quad (\text{B.7})$$

Integrating we get:

$$\int e^{-\frac{y^2 + 2iy\mu^2(\frac{p}{\hbar} - k_0)}{\mu^2}} dy = \frac{\sqrt{\pi}\mu}{2} e^{-\frac{\mu^2}{\hbar^2}(p - \hbar k_0)^2} \text{erf} \left[\frac{y}{\mu} + i \left(\frac{p\mu}{\hbar} - \mu k_0 \right) \right] \quad (\text{B.8})$$

Applying limits we get:

$$\int_{-\infty}^{\infty} e^{-\frac{y^2 + 2iy\mu^2(\frac{p}{\hbar} - k_0)}{\mu^2}} dy = \sqrt{\pi}\mu e^{-\frac{\mu^2}{\hbar^2}(p - \hbar k_0)^2} \quad (\text{B.9})$$

Substituting this back into the Wigner distribution (equation (B.2)) we finally get:

$$W(p, R) = \frac{1}{\pi\hbar} e^{-\frac{(R-R_0)^2}{\mu^2}} e^{-\frac{(p - \hbar k_0)^2}{\hbar^2/\mu^2}} \quad (\text{B.10})$$

Taking the maringal integrals we get the position and velocity probability distributions:

$$|f(R)|^2 = \frac{2}{\mu\sqrt{\pi}} e^{-\frac{(R-R_0)^2}{\mu^2}} \quad (\text{B.11})$$

$$|f(p)|^2 = \frac{2}{\frac{\hbar}{\mu}\sqrt{\pi}} e^{-\frac{\mu^2}{\hbar^2}(p - \hbar k_0)^2} \quad (\text{B.12})$$

The above distributions are randomly sampled to get initial atomic velocities and positions for each simulation.

Appendix C

$\mathbf{R}_{lk,v}$ Alternatives

C.1 $\mathbf{R}_{lk,v}$ Extrapolation

C.2 Alternative Quantum Momentum Intercept

In Agostini, 16² another quantum momentum intercept term is discussed. This term is not used because, as previously discussed in section 1.4, it leads to unphysical transfer of population between adiabatic states when the nonadiabatic coupling elements are 0. However, it can be used in these Tully Models as an effective fix to the discontinuities caused by the $\mathbf{R}_{lk,v}$ term.

The other quantum momentum intercept, $\mathbf{R}_{0,v}^{(I)}$, comes directly from the construction of the nuclear density using a linear combination of a product of gaussians (see equation (1.12) in the introduction). It is defined as in equation (C.1) below:

$$\mathbf{R}_{0,v}^{(I)} = \sum_J^{N_{tr}} \left[\frac{\hbar \prod_{v'} g_{\sigma_{v'}^{(J)}(t)} \left(\mathbf{R}_{v'}^{(I)}(t) - \mathbf{R}_{v'}^{(J)}(t) \right)}{2 \sigma_v^{(J)}(t)^2 \sum_K^{N_{tr}} \prod_{v'} g_{\sigma_{v'}^{(K)}(t)} \left(\mathbf{R}_{v'}^{(I)}(t) - \mathbf{R}_{v'}^{(K)}(t) \right)} \mathbf{R}_v^{(I)} \right] \quad (\text{C.1})$$

Appendix D

Rabi Oscillation

The time dependant Schrödinger equation is given below:

$$\hbar \frac{\delta}{\delta t} \Phi(\mathbf{R}(t), t) = \hat{H}(\mathbf{R}(t), t) \Phi(\mathbf{R}(t), t) \quad (\text{D.1})$$

If we hold the nuclear coordinates in place (e.g. remove time-dependence from nuclear coordinates) we get an ordinary differential equation as shown below:

$$\hbar \frac{d}{dt} \Phi(\mathbf{R}, t) = \hat{H}(\mathbf{R}, t) \Phi(\mathbf{R}, t) \quad (\text{D.2})$$

This has the following general solution.

$$\Phi(\mathbf{R}, t) = e^{\frac{i}{\hbar} \hat{H} t} \Phi(\mathbf{R}, 0)$$

Appendix E

Norm Conservation in CTMQC and Ehrenfest

A statement of the conservation of the norm, for a single trajectory, is given below in equation (E.1)

$$\frac{d}{dt} \sum_l |C_l(t)|^2 = \sum_l C_l^*(t) \frac{dC_l(t)}{dt} + \frac{dC_l^*(t)}{dt} C_l(t) = 0 \quad (\text{E.1})$$

Because the adiabatic populations are real we can remove any imaginary parts.

$$\frac{d}{dt} \sum_l |C_l(t)|^2 = 2\mathbb{R} \left[C_l^*(t) \frac{dC_l(t)}{dt} \right] \quad (\text{E.2})$$

Substituting the equation for the evolution of the adiabatic coefficients (and removing the purely imaginary term) into (E.2) we get equation (E.4)

$$\frac{d}{dt} \sum_l |C_l(t)|^2 = 2 \sum_l \mathbb{R} \left[\cancel{\frac{-i}{\hbar} \epsilon_{BO}^l C_l(t)^* \overline{C_l(t)}} - \sum_k \left[C_l(t)^* C_k(t) d_{lk}^{ad} - (A_l - B_l) C_l(t)^* C_l(t) \right] \right] \quad (\text{E.3})$$

$$= -2 \sum_l \mathbb{R} \left[\sum_k \left[C_l(t)^* C_k(t) d_{lk}^{ad} - (A_l - B_l) C_l(t)^* C_l(t) \right] \right] \quad (\text{E.4})$$

Where:

$$A_l = \sum_{v=1}^{N_n} \sum_k \frac{\mathcal{Q}_{lk,v}(t)}{\hbar M_v} \cdot \mathbf{f}_{k,v}(t) |C_k(t)|^2 \quad (\text{E.5})$$

$$B_l = \sum_{v=1}^{N_n} \sum_k \frac{\mathcal{Q}_{lk,v}(t)}{\hbar M_v} \cdot \mathbf{f}_{l,v}(t) |C_k(t)|^2 \quad (\text{E.6})$$

The NACE term evaluates to 0 due to the anti-symmetry of the NACE giving us equation (E.8).

So far, we have proved that the norm should be conserved here for all terms apart from the quantum momentum terms i.e. Ehrenfest.

$$\frac{d}{dt} \sum_l \left| C_l^{QM}(t) \right|^2 = 2 \sum_l \mathbb{R} [(A_l - B_l) C_l(t)^* C_l(t)] \quad (\text{E.7})$$

$$= 2 \left[\sum_l A_l |C_l(t)|^2 - \sum_l B_l |C_l(t)|^2 \right] \quad (\text{E.8})$$

However, $\sum_l A_l |C_l|^2 \equiv \sum_l B_l |C_l|^2$, therefore there is no change in the population and the norm should be conserved.

Appendix F

Adiabatic State Initialisation

By diagonalising the Hamiltonian we get the adiabatic energies (eigenvalues) for each state and transformation matrix (eigenvectors) to calculate diabatic states \mathbb{U} . We can calculate diabatic coefficients corresponding to each adiabatic state via equation (F.1) below.

$$\mathbb{U}\mathbf{C}_n = \mathbf{u}_n \quad (\text{F.1})$$

Where \mathbb{U} is the transformation matrix of size $(N_{\text{mol}}, N_{\text{mol}})$, \mathbf{C} is a complex vector of size N_{mol} containing coefficients for adiabatic state n and \mathbf{u} is a complex vector of size N_{mol} containing coefficients for diabatic state n .

Seeing as we would like to find the diabatic population corresponding to each adiabatic state we localise coefficients on each pure adiabatic state and carry out the transformation e.g: $C_i = (1+0i, 0+0i, 0+0i, \dots)$ when we want to find the diabatic coefficient corresponding to state 1 and $C_i = (0+0i, 1+0i, 0+0i, \dots)$ when we want to find the diabatic coefficient corresponding to state 2 etc.. Therefore, the column, n , of the transformation matrix, \mathbb{U} , gives the diabatic coefficients corresponding to adiabatic state, n , as shown below in equation (F.2)

$$U_{in} = u_i \quad (\text{F.2})$$

Where n is the adiabatic state index and i is the diabatic (molecular) state index.

Once we have the diabatic state corresponding to each adiabatic state, and the en-

ergy of that adiabatic state, we can find which state best fulfills the requirements of being close to the center of the system and being within $3KT$ of the ground state. In order to do this, we can loop over each adiabatic state in increasing order of energy. The center of the system is calculated and the population weighted average center of mass, \mathbf{R}_n of the diabatic coefficients corresponding to adiabatic state n is calculated as in equation (F.3).

$$\mathbf{R}_n = \sum_i |u_i|^2 \mathbf{R}_{COM,i} \quad (\text{F.3})$$

The Euclidean distance between the center of the system and $\mathbf{R}_{COM,i}$ is calculated and if this distance is below some threshold value then we initialise the surface hopping trajectory on that adiabatic state. If we do not find any states within $3KT$ of the ground state and within an acceptable radius of the center we start again this time increasing the maximum allowed distance from the center. If this maximum allowed distance is increased such that we reach another threshold distance the energy threshold is increased this time until a state is found that is close enough to the center. In this way we find an adiabatic state, which when transformed, gives a diabatic population close to center of the system and near the ground state energy.

Appendix G

Colophon

This is a description of the tools you used to make your thesis. It helps people make future documents, reminds you, and looks good.

(example) This document was set in the Times Roman typeface using L^AT_EX (specifically LuaTeX) and BibT_EX, composed with Vim Used Archer, Kathleen etc...

Bibliography

- [1] Federica Agostini, Ali Abedi, Yasumitsu Suzuki, Seung Kyu Min, Neepta T. Maitra, and E. K. U. Gross. The exact forces on classical nuclei in non-adiabatic charge transfer. *The Journal of Chemical Physics*, 142(8):084303, February 2015.
- [2] Federica Agostini, Seung Kyu Min, Ali Abedi, and E. K. U. Gross. Quantum-Classical Nonadiabatic Dynamics: Coupled- vs Independent-Trajectory Methods. *Journal of Chemical Theory and Computation*, 12(5):2127–2143, May 2016.
- [3] Graeme H. Gossel, Federica Agostini, and Neepta T. Maitra. Coupled-Trajectory Mixed Quantum-Classical Algorithm: A Deconstruction. *Journal of Chemical Theory and Computation*, August 2018.
- [4] William Humphrey, Andrew Dalke, and Klaus Schulten. VMD – Visual Molecular Dynamics. *Journal of Molecular Graphics*, 14:33–38, 1996.
- [5] John Stone. An Efficient Library for Parallel Ray Tracing and Animation. Master’s thesis, Computer Science Department, University of Missouri-Rolla, April 1998.
- [6] C. K. Chiang, C. R. Fincher, Y. W. Park, A. J. Heeger, H. Shirakawa, E. J. Louis, S. C. Gau, and Alan G. MacDiarmid. Electrical Conductivity in Doped Polyacetylene. *Physical Review Letters*, 39(17):1098–1101, October 1977.
- [7] Hideki Shirakawa, Edwin J. Louis, Alan G. MacDiarmid, Chwan K. Chiang, and Alan J. Heeger. Synthesis of electrically conducting organic polymers: halogen derivatives of polyacetylene, $(\text{CH})_x$. *J. Chem. Soc., Chem. Commun.*, 0(16):578–580, Jan 1977.

- [8] Bernard Kippelen and Jean-Luc Brédas. Organic photovoltaics. *Energy Environ. Sci.*, 2(3):251–261, 2009.
- [9] M. J. Małachowski and J. Źmija. Organic field-effect transistors. *Opto-Electron. Rev.*, 18(2):121–136, Jun 2010.
- [10] N. Thejo Kalyani and S. J. Dhoble. Organic light emitting diodes: Energy saving lighting technology—A review. *Renewable Sustainable Energy Rev.*, 16(5):2696–2723, Jun 2012.
- [11] Sebastian Reineke, Frank Lindner, Gregor Schwartz, Nico Seidler, Karsten Walzer, Björn Lüssem, and Karl Leo. White organic light-emitting diodes with fluorescent tube efficiency. *Nature*, 459(7244):234, May 2009.
- [12] Kazuki Kato, Toshihiko Iwasaki, and Takatoshi Tsujimura. Over 130 lm/w all-phosphorescent white oleds for next-generation lighting. *Journal of Photopolymer Science and Technology*, 28:335–340, 10 2015.
- [13] Veaceslav Coropceanu, Jérôme Cornil, Demetrio A. da Silva Filho, Yoann Olivier, Robert Silbey, and Jean-Luc Brédas. Charge Transport in Organic Semiconductors. *Chemical Reviews*, 107(4):926–952, April 2007.
- [14] Samuele Giannini, Antoine Carof, Matthew Ellis, Hui Yang, Orestis George Zio-gos, Soumya Ghosh, and Jochen Blumberger. Quantum localization and delocaliza-tion of charge carriers in organic semiconducting crystals. *Nature Communications*, 10(1):3843, Aug 2019.
- [15] Alessandro Troisi. Charge transport in high mobility molecular semiconductors: classical models and new theories. *Chem. Soc. Rev.*, 40:2347–2358, 2011.
- [16] Simone Fratini, Didier Mayou, and Sergio Ciuchi. The transient localization scenario for charge transport in crystalline organic materials. *Advanced Functional Materials*, 26(14):2292–2315, 2016.

- [17] I. Yavuz. Dichotomy between the band and hopping transport in organic crystals: insights from experiments. *Physical Chemistry Chemical Physics*, 19(38):25819–25828, 2017.
- [18] J. S. Brown and S. E. Shaheen. Introducing correlations into carrier transport simulations of disordered materials through seeded nucleation: impact on density of states, carrier mobility, and carrier statistics. *J. Phys.: Condens. Matter*, 30(13):135702, Mar 2018.
- [19] Tino Zimmerling and Bertram Batlogg. Improving charge injection in high-mobility rubrene crystals: From contact-limited to channel-dominated transistors. *Journal of Applied Physics*, 115(16):164511, 2014.
- [20] V. Podzorov, E. Menard, A. Borissov, V. Kiryukhin, J. A. Rogers, and M. E. Gershenson. Intrinsic charge transport on the surface of organic semiconductors. *Phys. Rev. Lett.*, 93:086602, Aug 2004.
- [21] Samuele Giannini, Antoine Carof, and Jochen Blumberger. Crossover from Hopping to Band-Like Charge Transport in an Organic Semiconductor Model: Atomistic Nonadiabatic Molecular Dynamics Simulation. *The Journal of Physical Chemistry Letters*, 9(11):3116–3123, June 2018.
- [22] Harald Oberhofer, Karsten Reuter, and Jochen Blumberger. Charge Transport in Molecular Materials: An Assessment of Computational Methods. *Chemical Reviews*, 117(15):10319–10357, August 2017.
- [23] John C. Tully. *Nonadiabatic Dynamics*. pages 34–71.
- [24] Simone Pisana, Michele Lazzeri, Cinzia Casiraghi, Kostya S. Novoselov, A. K. Geim, Andrea C. Ferrari, and Francesco Mauri. Breakdown of the adiabatic Born–Oppenheimer approximation in graphene. *Nat. Mater.*, 6(3):198, Feb 2007.
- [25] M. Born and R. Oppenheimer. Zur Quantentheorie der Molekeln. *Ann. Phys.*, 389(20):457–484, Jan 1927.

- [26] Sharon Hammes-Schiffer. Theoretical Perspectives on Proton-Coupled Electron Transfer Reactions. *Acc. Chem. Res.*, 34(4):273–281, Apr 2001.
- [27] Sharon Hammes-Schiffer and John C. Tully. Proton transfer in solution: Molecular dynamics with quantum transitions. *J. Chem. Phys.*, 101(6):4657–4667, Sep 1994.
- [28] My Hang V. Huynh and Thomas J. Meyer. Proton-coupled electron transfer. *Chemical Reviews*, 107(11):5004–5064, Nov 2007.
- [29] John C. Tully. Nonadiabatic molecular dynamics. *International Journal of Quantum Chemistry*, 40(S25):299–309, 1991.
- [30] Raymond Kapral and Giovanni Ciccotti. Mixed quantum-classical dynamics. *J. Chem. Phys.*, 110(18):8919–8929, May 1999.
- [31] Todd J. Martínez*. Insights for Light-Driven Molecular Devices from Ab Initio Multiple Spawning Excited-State Dynamics of Organic and Biological Chromophores. American Chemical Society, Oct 2005.
- [32] Guillermo Albareda, Heiko Appel, Ignacio Franco, Ali Abedi, and Angel Rubio. Correlated Electron-Nuclear Dynamics with Conditional Wave Functions. *Phys. Rev. Lett.*, 113(8):083003, Aug 2014.
- [33] John C. Tully. Molecular dynamics with electronic transitions. *J. Chem. Phys.*, 93(2):1061–1071, Jul 1990.
- [34] R. L et al Whetten. Molecular dynamics beyond the adiabatic approximation: New experiments and theory. *Ann. Rev. Phys. Chem.*, 36:277–320.
- [35] Neil Shenvi, Joseph E. Subotnik, and Weitao Yang. Simultaneous-trajectory surface hopping: A parameter-free algorithm for implementing decoherence in nonadiabatic dynamics. *J. Chem. Phys.*, 134(14):144102, Apr 2011.
- [36] D. F. Coker and L. Xiao. Methods for molecular dynamics with nonadiabatic transitions. *J. Chem. Phys.*, 102(1):496–510, Jan 1995.

- [37] Joseph E. Subotnik, Amber Jain, Brian Landry, Andrew Petit, Wenjun Ouyang, and Nicole Bellonzi. Understanding the surface hopping view of electronic transitions and decoherence. *Annual Review of Physical Chemistry*, 67(1):387–417, 2016. PMID: 27215818.
- [38] Giovanni Granucci, Maurizio Persico, and Alberto Zocante. Including quantum decoherence in surface hopping. *The Journal of Chemical Physics*, 133(13):134111, 2010.
- [39] Heather M. Jaeger, Sean Fischer, and Oleg V. Prezhdo. Decoherence-induced surface hopping. *The Journal of Chemical Physics*, 137(22):22A545, 2012.
- [40] Amber Jain, Ethan Alguire, and Joseph E. Subotnik. An efficient, augmented surface hopping algorithm that includes decoherence for use in large-scale simulations. *Journal of Chemical Theory and Computation*, 12(11):5256–5268, Nov 2016.
- [41] Joseph E. Subotnik and Neil Shenvi. A new approach to decoherence and momentum rescaling in the surface hopping algorithm. *The Journal of Chemical Physics*, 134(2):024105, 2011.
- [42] Xiaosong Li, John C. Tully, H. Bernhard Schlegel, and Michael J. Frisch. Ab initio Ehrenfest dynamics. *J. Chem. Phys.*, 123(8):084106, Aug 2005.
- [43] Kenichiro Saita and Dmitrii V. Shalashilin. On-the-fly ab initio molecular dynamics with multiconfigurational Ehrenfest method. *J. Chem. Phys.*, 137(22):22A506, Dec 2012.
- [44] Daniela Kohen, Frank H. Stillinger, and John C. Tully. Model studies of nonadiabatic dynamics. *J. Chem. Phys.*, 109(12):4713–4725, Sep 1998.
- [45] John C. Tully. Perspective: Nonadiabatic dynamics theory. *The Journal of Chemical Physics*, 137(22):22A301, December 2012.
- [46] Priya V. Parandekar and John C. Tully. Detailed Balance in Ehrenfest Mixed Quantum-Classical Dynamics. *Journal of Chemical Theory and Computation*, 2(2):229–235, March 2006.

- [47] Ali Abedi, Neepa T. Maitra, and E. K. U. Gross. Exact Factorization of the Time-Dependent Electron-Nuclear Wave Function. *Physical Review Letters*, 105(12), September 2010.
- [48] Federica Agostini, Seung Kyu Min, and E. K. U. Gross. Semiclassical analysis of the electron-nuclear coupling in electronic non-adiabatic processes. *Annalen der Physik*, 527(9-10):546–555, October 2015.
- [49] Federica Agostini, Ali Abedi, Yasumitsu Suzuki, and E.K.U. Gross. Mixed quantum-classical dynamics on the exact time-dependent potential energy surface: a fresh look at non-adiabatic processes. *Molecular Physics*, 111(22-23):3625–3640, December 2013.
- [50] Ali Abedi, Federica Agostini, Yasumitsu Suzuki, and E. K. U. Gross. Dynamical Steps that Bridge Piecewise Adiabatic Shapes in the Exact Time-Dependent Potential Energy Surface. *Physical Review Letters*, 110(26), June 2013.
- [51] Seung Kyu Min, Ali Abedi, Kwang S. Kim, and E. K. U. Gross. Is the Molecular Berry Phase an Artifact of the Born-Oppenheimer Approximation? *Phys. Rev. Lett.*, 113(26):263004, Dec 2014.
- [52] Farnaz A. Shakib and Pengfei Huo. Ring Polymer Surface Hopping: Incorporating Nuclear Quantum Effects into Nonadiabatic Molecular Dynamics Simulations. *J. Phys. Chem. Lett.*, 8(13):3073–3080, Jul 2017.
- [53] Basile F. E. Curchod, Ivano Tavernelli, and Ursula Rothlisberger. Trajectory-based solution of the nonadiabatic quantum dynamics equations: an on-the-fly approach for molecular dynamics simulations. *PCCP*, 13(8):3231–3236, Feb 2011.
- [54] Ivano Tavernelli. Ab initio-driven trajectory-based nuclear quantum dynamics in phase space. *Phys. Rev. A*, 87(4):042501, Apr 2013.
- [55] Arne Scherrer, Federica Agostini, Daniel Sebastiani, E. K. U. Gross, and Rodolphe Vuilleumier. Nuclear velocity perturbation theory for vibrational circular dichroism:

- An approach based on the exact factorization of the electron-nuclear wave function. *J. Chem. Phys.*, 143(7):074106, Aug 2015.
- [56] Seung Kyu Min, Federica Agostini, Ivano Tavernelli, and E. K. U. Gross. Ab Initio Nonadiabatic Dynamics with Coupled Trajectories: A Rigorous Approach to Quantum (De)Coherence. *The Journal of Physical Chemistry Letters*, 8(13):3048–3055, July 2017.
- [57] John C. Tully. Molecular dynamics with electronic transitions. *The Journal of Chemical Physics*, 93(2):1061–1071, July 1990.
- [58] Fruzsina Gajdos, Siim Valner, Felix Hoffmann, Jacob Spencer, Marian Breuer, Adam Kubas, Michel Dupuis, and Jochen Blumberger. Ultrafast Estimation of Electronic Couplings for Electron Transfer between π -Conjugated Organic Molecules. *Journal of Chemical Theory and Computation*, 10(10):4653–4660, October 2014.
- [59] J. VandeVondele, J; Hutter. Gaussian basis sets for accurate calculations on molecular systems in gas and condensed phases. *The Journal of Chemical Physics*, 127(11).
- [60] J. Spencer, F. Gajdos, and J. Blumberger. FOB-SH: Fragment orbital-based surface hopping for charge carrier transport in organic and biological molecules and materials. *The Journal of Chemical Physics*, 145(6):064102, August 2016.
- [61] Antoine Carof, Samuele Giannini, and Jochen Blumberger. Detailed balance, internal consistency, and energy conservation in fragment orbital-based surface hopping. *The Journal of Chemical Physics*, 147(21):214113, December 2017.
- [62] Biswajit Ray, Aditya G. Baradwaj, Bryan W. Boudouris, and Muhammad A. Alam. Defect characterization in organic semiconductors by forward bias capacitance–voltage (fb-cv) analysis. *The Journal of Physical Chemistry C*, 118(31):17461–17466, Aug 2014.
- [63] W. S. Hu, Y. T. Tao, Y. J. Hsu, D. H. Wei, and Y. S. Wu. Molecular orientation of evaporated pentacene films on gold: alignment effect of self-assembled monolayer. *Langmuir*, 21(6):2260–2266, Mar 2005.

- [64] Tatsuo Hasegawa and Jun Takeya. Organic field-effect transistors using single crystals. *Science and Technology of Advanced Materials*, 10(2):024314, 2009.
- [65] John E. Anthony, James S. Brooks, David L. Eaton, and Sean R. Parkin. Functionalized pentacene: improved electronic properties from control of solid-state order. *Journal of the American Chemical Society*, 123(38):9482–9483, Sep 2001.
- [66] John E. Anthony, David L. Eaton, and Sean R. Parkin. A road map to stable, soluble, easily crystallized pentacene derivatives. *Organic Letters*, 4(1):15–18, Jan 2002.
- [67] A. D’Angelo, B. Edgar, A. P. Hurt, and M. D. Antonijević. Physico-chemical characterisation of three-component co-amorphous systems generated by a melt-quench method. *Journal of Thermal Analysis and Calorimetry*, 134(1):381–390, Oct 2018.
- [68] Wanderlã L. Scopel, Antônio J. R. da Silva, and A. Fazzio. Amorphous hfo_2 and $\text{hf}_{1-x}\text{si}_x\text{O}$ via a melt-and-quench scheme using ab initio molecular dynamics. *Phys. Rev. B*, 77:172101, May 2008.
- [69] Seth S. Berbano, Inseok Seo, Christian M. Bischoff, Katherine E. Schuller, and Steve W. Martin. Formation and structure of $\text{na}_2\text{s}+\text{p}_2\text{s}_5$ amorphous materials prepared by melt-quenching and mechanical milling. *Journal of Non-Crystalline Solids*, 358(1):93 – 98, 2012.
- [70] Pranav Karmwar, Kirsten Graeser, Keith C. Gordon, Clare J. Strachan, and Thomas Rades. Investigation of properties and recrystallisation behaviour of amorphous indomethacin samples prepared by different methods. *International Journal of Pharmaceutics*, 417(1):94 – 100, 2011. Advanced characterization techniques.
- [71] Min-Jin Ko, Joel Plawsky, and Meyer Birnboim. Fabrication of cds/ag hybrid quantum dot composites using a melt/quench method. *Journal of Non-Crystalline Solids*, 203:211 – 216, 1996. Optical and Electrical Properties of Glasses.
- [72] Steve Plimpton. Fast parallel algorithms for short-range molecular dynamics. *Journal of Computational Physics*, 117(1):1 – 19, 1995.

- [73] Steve Plimpton. LAMMPS software. <http://lammps.sandia.gov>, 1995. [Online; accessed 21-Jan-2021].
- [74] Steve Plimpton, Roy Pollock, and Mark Stevens. Particle-mesh ewald and rrespa for parallel molecular dynamics simulations. In *Proceedings of the Eighth SIAM Conference on Parallel Processing for Scientific Computing*, 1997.
- [75] Christopher I. Bayly, Piotr Cieplak, Wendy Cornell, and Peter A. Kollman. A well-behaved electrostatic potential based method using charge restraints for deriving atomic charges: the resp model. *The Journal of Physical Chemistry*, 97(40):10269–10280, Oct 1993.
- [76] M. J. Frisch, G. W. Trucks, H. B. Schlegel, G. E. Scuseria, M. A. Robb, J. R. Cheeseman, G. Scalmani, V. Barone, G. A. Petersson, H. Nakatsuji, X. Li, M. Caricato, A. V. Marenich, J. Bloino, B. G. Janesko, R. Gomperts, B. Mennucci, H. P. Hratchian, J. V. Ortiz, A. F. Izmaylov, J. L. Sonnenberg, D. Williams-Young, F. Ding, F. Lipparini, F. Egidi, J. Goings, B. Peng, A. Petrone, T. Henderson, D. Ranasinghe, V. G. Zakrzewski, J. Gao, N. Rega, G. Zheng, W. Liang, M. Hada, M. Ehara, K. Toyota, R. Fukuda, J. Hasegawa, M. Ishida, T. Nakajima, Y. Honda, O. Kitao, H. Nakai, T. Vreven, K. Throssell, J. A. Montgomery, Jr., J. E. Peralta, F. Ogliaro, M. J. Bearpark, J. J. Heyd, E. N. Brothers, K. N. Kudin, V. N. Staroverov, T. A. Keith, R. Kobayashi, J. Normand, K. Raghavachari, A. P. Rendell, J. C. Burant, S. S. Iyengar, J. Tomasi, M. Cossi, J. M. Millam, M. Klene, C. Adamo, R. Cammi, J. W. Ochterski, R. L. Martin, K. Morokuma, O. Farkas, J. B. Foresman, and D. J. Fox. Gaussian~16 Revision C.01, 2016. Gaussian Inc. Wallingford CT.
- [77] Junmei Wang, Romain M. Wolf, James W. Caldwell, Peter A. Kollman, and David A. Case. Development and testing of a general amber force field. *Journal of Computational Chemistry*, 25(9):1157–1174, 2004.
- [78] Makoto Yoneya, Masahiro Kawasaki, and Masahiko Ando. Molecular dynamics simulations of pentacene thin films: The effect of surface on polymorph selection. *J. Mater. Chem.*, 20:10397–10402, 2010.

- [79] Makoto Yoneya, Masahiro Kawasaki, and Masahiko Ando. Are pentacene monolayer and thin-film polymorphs really substrate-induced? a molecular dynamics simulation study. *The Journal of Physical Chemistry C*, 116(1):791–795, Jan 2012.
- [80] Makoto Yoneya. Simulation of crystallization of pentacene and its derivatives from solution. *The Journal of Physical Chemistry C*, Jan 2021.
- [81] Ryan A. Miller, Amanda Larson, and Karsten Pohl. Novel surface diffusion characteristics for a robust pentacene derivative on au(111) surfaces. *Chemical Physics Letters*, 678:28 – 34, 2017.
- [82] Dong Wang, Ling Tang, Mengqiu Long, and Zhigang Shuai. Anisotropic thermal transport in organic molecular crystals from nonequilibrium molecular dynamics simulations. *The Journal of Physical Chemistry C*, 115(13):5940–5946, Apr 2011.
- [83] Florian Steiner, Carl Poelking, Dorota Niedzialek, Denis Andrienko, and Jenny Nelson. Influence of orientation mismatch on charge transport across grain boundaries in tri-isopropylsilylethynyl (tips) pentacene thin films. *Phys. Chem. Chem. Phys.*, 19:10854–10862, 2017.
- [84] Ida Bagus Hendra Prastiawan, Jingxiang Xu, Yusuke Ootani, Yuji Higuchi, Nobuki Ozawa, Shingo Maruyama, Yuji Matsumoto, and Momoji Kubo. Molecular interactions between pentacene and imidazolium ionic liquids: A molecular dynamics study. *Chemistry Letters*, 47(9):1154–1157, 2018.
- [85] EPA DSSTox. Epa dsstox. <https://comptox.epa.gov/dashboard/DTXSID7059648>, 2021. [Online; accessed 25-Jan-2021].
- [86] Stefan Schiefer, Martin Huth, Alexander Dobrinevski, and Bert Nickel. Determination of the crystal structure of substrate-induced pentacene polymorphs in fiber structured thin films. *Journal of the American Chemical Society*, 129(34):10316–10317, Aug 2007.
- [87] Martin Ester, Hans-Peter Kriegel, Jörg Sander, and Xiaowei Xu. A density-based

algorithm for discovering clusters in large spatial databases with noise. pages 226–231. AAAI Press, 1996.